MDPI

Article

Kinetic Analysis of Oxygen Evolution on Spin-Coated Thin-Film Electrodes via Electrochemical Impedance Spectroscopy

Yu-Wei Lin [1,†], Yi-Syuan Li [1,†], Chun-Wei Chang [1], Li-Cheng Huang [1], Tai-Hsin Yin [1], Yu-Ting Liu [1], Dong Kyoo Park [2], Changsik Choi [2,*] and YongMan Choi [1,*]

1　College of Photonics, National Yang Ming Chiao Tung University, Tainan 71150, Taiwan; ywlin0911.pt09@nycu.edu.tw (Y.-W.L.); shiuan3098.pt09@nycu.edu.tw (Y.-S.L.); winerchang7.pt10@nycu.edu.tw (C.-W.C.); qdeaws345.pt11@nycu.edu.tw (L.-C.H.); taihsin.pt09@nycu.edu.tw (T.-H.Y.); david19961104@gmail.com (Y.-T.L.)
2　Clean Energy Conversion Research Center, Institute for Advanced Engineering, Yongin 17180, Republic of Korea; parkdk@iae.re.kr
*　Correspondence: cschoi@iae.re.kr (C.C.); ymchoi@nycu.edu.tw (Y.C.)
†　These authors contributed equally to this work.

Abstract: Sustainable and renewable energy technologies have attracted significant attention for reducing greenhouse emissions in the shift from fossil fuels. The production of green hydrogen from water electrolysis is considered an environmentally friendly strategy for a decarbonized economy. We examine the activities of the hydrogen and oxygen evolution reactions (HER and OER) using spin-coated thin-film electrodes with Pt/C and IrO_2 nano-electrocatalysts under acidic conditions. The nano-electrocatalysts are characterized using scanning electron microscopy (SEM), X-ray diffraction (XRD), and atomic force microscopy (AFM). The electrocatalytic activities of nanoscale Pt/C and IrO_2 are close to those of commercial Pt/C and superior to commercial IrO_2, resulting in improved overall water splitting performance. Furthermore, the OER kinetics analysis using the IrO_2 electrode is conducted using EIS measurements with distribution of relaxation time (DRT) analysis, resulting in a comparable exchange current density to that from the Tafel slope method (6.7×10^{-2} mA/cm^2 versus 5.1×10^{-2} mA/cm^2), demonstrating the validity of the kinetics analysis. This work provides a general strategy for preparing novel and highly active OER electrode materials for water electrolysis.

Keywords: water electrolysis; thin films; kinetic analysis; electrochemical impedance spectroscopy

1. Introduction

Green hydrogen production is considered a significant solution for achieving net-zero greenhouse gas emissions, as hydrogen is the cleanest energy carrier for transportation and industry [1]. Green hydrogen is mainly produced using water electrolyzers powered by renewable energy. Because the performance of water electrolysis devices is limited by the ohmic drop and the overpotential [2,3], developing novel efficient electrocatalysts for the hydrogen and oxygen evolution reactions (HER and OER) with low ohmic drop and overpotential is pivotal [4–8]. Furthermore, designing novel, highly efficient electrocatalysts with acid tolerance is also vital for proton exchange membrane (PEM) water electrolysis [9]. For the HER, protons in the solution are transferred to the electrode surface to combine with electrons, producing hydrogen [6]. Although platinum-based catalysts (i.e., Pt/C) are the most active HER electrode materials in water electrolysis, their high cost and limited abundance have hindered large-scale applications. For the OER, the characteristics of the four-electron transfer and the complex electrocatalytic process [10–13] significantly affect conversion efficiencies. Iridium-based electrocatalysts (i.e., IrO_2) are widely used due to their high OER activity and bifunctionality [14–20]. Accordingly, developing highly

efficient OER electrode materials has attracted significant attention due to their sluggish reaction kinetics [21,22]. Numerous studies have been conducted to elucidate the reaction mechanisms of water splitting at electrode surfaces [23–25]. Simulating reaction kinetics for estimating kinetic parameters is essential for investigating the reaction process and electro-catalytic activities [26]. Typically, the Tafel extrapolation method is applied by determining the exchange current density (j_0) of the OER through Tafel plots ($\eta = a + b \cdot \log(j)$) [27], where η, b, and j are the overpotential, the Tafel slope, and the current density, respectively. On the other hand, Costa et al. reported an OER kinetic analysis of a lead (Pb) electrode using electrochemical impedance spectroscopy (EIS) [28]. Lu et al. then applied the approach to obtain OER kinetic parameters with microkinetic modeling on a rhodium (Rh) electrode [26]. In this study, nanoscale IrO_2 electrocatalysts were synthesized to verify their applicability in water electrolysis with nano-sized Pt/C. We applied the spin-coating method to attain reproducible electrochemical activities of the as-synthesized Pt/C and IrO_2 on fluorine-doped tin oxide (FTO) glass substrates owing to their reasonable electrical conductivities and excellent stability in acidic media [29,30]. Kinetic analysis using electro-chemical impedance spectroscopy (EIS) is a powerful tool to investigate the fundamental mechanisms and kinetics of electrochemical reactions at electrode/electrolyte interfaces. Then, to experimentally understand the OER kinetic process and parameters of nanoscale IrO_2 electrode materials, EIS measurements with the equivalent electrical circuit (EEC) analysis were conducted [26]. Furthermore, the distribution of relaxation time (DRT) analysis was also used to investigate the contribution of the impedance of the electrochemical process evolution on the OER electrode surfaces [31,32]. In particular, we found that the exchange current density obtained from the EIS-based kinetic analysis agrees well with that from the Tafel slope method. This study supports the validity of the microkinetic model for OER processes [26].

2. Experimental Details

2.1. Electrocatalyst Synthesis and Fabrication of Thin-Film Electrodes

$PtCl_4$ (99.9%, Alfa Aesar, Ward Hill, MA, USA), $(NH_4)_2(IrCl_6)$ (99%, Sigma-Aldrich, Burlington, MA, USA), $NaNO_3$ (99.5%, Alfa Aesar, Ward Hill, MA, USA), 0.1 M $HClO_4$ (Acros Organics BVBA, Geel, Belgium), 5 wt.% Nafion solution (Sigma-Aldrich, Burlington, MA, USA), and Vulcan XC-72 (Cabot Corporation, Boston, MA, USA) were used without further purification. Fuel-cell-grade Pt/C (20 wt.%, Fuel Cell Store, Bryan, TX, USA) and IrO_2 (99%, Alfa Aesar, Ward Hill, MA, USA) were used as active benchmark electrocatalysts for the HER and OER. Carbon-supported Pt electrocatalysts (20 wt.% Pt/C) were synthesized based on a previous approach [33]. The precursor Pt salt (50.5 mg of $PtCl_4$) was mixed with carbon blacks (Vulcan XC-72) in 50 mL of acetone (99.5%, Anaqua Chemical Supply, Houston, TX, USA) and stirred for 1 h, followed by a 30 min ultrasonication and drying at 50 °C on a hot place with stirring. Then, dried samples were annealed at 600 °C in 15% H_2/Ar for 2 h. Also, nanoscale IrO_2 powders were prepared using a modified Adams fusion method [34]. An amount of 206.7 mg of $(NH_4)_2(IrCl_6)$ was dissolved in 6.7 mL of isopropyl alcohol (IPA) (99.5%, Anaqua Chemical Supply, Houston, TX, USA) and stirred for 30 min, followed by adding $NaNO_3$ powders to the solution with an additional 30 min stirring with a weight ratio of $NaNO_3/(NH_4)_2(IrCl_6) \sim 10$ [34]. The effective removal of potential contaminants (i.e., NaCl) was verified in previous studies [34,35].

Then, samples were filtered using Isopore membrane filters (Millipore, MA, USA) with a pore size of 0.4 μm. Collected samples were dried in an oven for 30 min at 110 °C and calcined in a tube furnace (Thermo Scientific, Lindberg Blue M, Waltham, MA, USA) for 2 h at 350 °C in air. The collected samples were then washed via filtration with ~1.5 L of deionized (DI) water to remove impurities (i.e., unreacted precursor salts). IrO_2 nanoparticles were dried in an oven for 2 h at 100 °C before characterization. As shown in Figure 1, thin-film electrodes were prepared via the spin-coating method on fluorine-doped tin oxide glass substrates (FTO, ~400 nm and 1 cm × 2 cm). FTO substrates were first consecutively cleaned in an ultrasonic bath of acetone, IPA, ethanol, and DI water

for 5 min, then dried in an oven and subjected to UV ozone treatment for 20 min. A catalyst ink was prepared by mixing 3 mg of catalyst powders with 300 μL of IPA solution (volume ratio of DI water/IPA = 3) and 50 μL of 5 wt.% Nafion solution, followed by a 40 min ultrasonication in an ice bath. An amount of 10 μL catalyst ink was placed on an FTO substrate at 500 rpm for 30 s using a spin coater in a fume hood. An active area of 5 mm × 5 mm was set using a chemical-tolerant tape. The thin-film samples were dried in an oven at 70 °C for 30 min and then air-dried in a fume hood for 1 h.
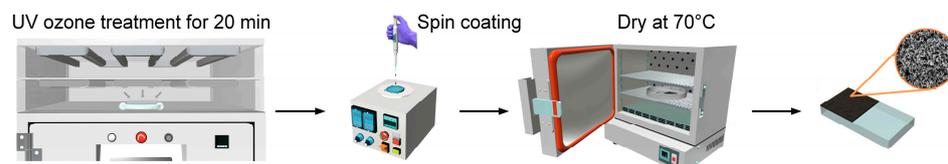
Figure 1. Schematic of the preparation process of thin-film electrodes on an FTO-coated glass substrate using spin-coating.

2.2. Materials' Characterization

Surface morphologies of the Pt/C thin film spin-coated on FTO were observed using scanning electron microscopy (SEM, Zeiss Gemini 450, Jena, Germany) operated at an acceleration voltage of 10 keV and atomic force microscopy (AFM, Bruker Innova, MA, USA) in tapping mode. X-ray diffraction (XRD, Brucker D8 DISCOVER, Billerica, MA, USA) with Cu Kα radiation (λ = 0.154184 nm) was applied to analyze as-prepared electrocatalysts (Pt/C and IrO$_2$). Electrochemical measurements were conducted using a potentiostat (SP-150e, BioLogic, Seyssinet-Pariset, France) with a typical three-electrode system in a 0.1 M HClO$_4$ electrolyte. In this study, an Ag/AgCl (3 M NaCl) reference electrode was used to measure potentials, which were converted to the reversible hydrogen electrode (RHE) scale using V_{RHE} = $V_{(Ag/AgCl)}$ + pH × 0.059 + 0.209, where $V_{(Ag/AgCl)}$ is the measured potential against the Ag/AgCl reference electrode [36]. A graphite rod was used as a counter electrode to avoid the influence of HER on the Pt coil owing to the electrochemical dissolution–deposition process of Pt [37]. Electrocatalysts were always conditioned using cyclic voltammetry (CV) cycling at 20 mV/s until they turned stable. Also, we evaluated the double-layer capacitance (C$_{dl}$) using scanning CVs at different scan rates (10, 25, 50, 75, and 100 mV/s) in a non-Faradaic OER potential range. The electrolyte solution was H$_2$- and O$_2$-saturated for HER and OER measurements to remove the excess gas from the electrolyte. iR-corrected polarization curves [38] were obtained using linear sweep voltammetry (LSV) at a scan rate of 5 mV/s. To examine the OER kinetic process, electrochemical impedance spectroscopy (EIS) was conducted from 1 MHz to 50 mHz with 5 mV sinusoidal amplitude with six data points per frequency decade at current densities of 2, 4, 6, 8, and 10 mA/cm^2.

## 3. Results and Discussion

3.1. Characterization of Thin-Film Electrodes

Figure 2a,b demonstrate surface morphologies of the Pt/C thin film using SEM. The thin-film morphology confirms that the spin-coating method provides a good dispersion of Pt/C on FTO, exhibiting a microporous structure. Figure 2c shows an AFM image of the Pt/C thin film whose morphology is similar to that produced using SEM (Figure 2b). The roughness value (R$_q$ = 65.2 nm) illustrates a high active area of the thin-film electrode, potentially leading to good HER activities, as reported [39,40]. The surface wettability of electrocatalysts was examined using a homemade contact angle measurement tool with a high-resolution camera by dropping 5 μL of DI water on the thin-film electrodes (0.5 cm × 0.5 cm) [41]. As displayed in Figure 2d, the contact angles of 134.2° (IrO$_2$) and 137.9° (Pt/C) indicate the hydrophobic behavior of the electrode materials on FTO [40], ensuring the low interaction of the generated gas bubbles [42,43]. Figure 2e shows the XRD patterns of the as-synthesized IrO$_2$ and Pt/C nanoparticles. The XRD analysis of IrO$_2$ verifies a rutile structure with an amorphous phase [44] without metallic iridium impurities.

The diffraction peaks of 39.7°, 46.2°, and 67.6° of Pt/C are assigned to the (111), (200), and (220) planes of the face-centered cubic (fcc) [45–48]. The Pt/C sample annealed at 600 °C in 15% H_2/Ar exhibits sharp and intense peaks caused by increased crystallization [49]. The peak observed around 24.5° in the XRD patterns is attributed to the graphitic (002) plane of Vulcan XC-72 [50]. The average crystallite sizes (D) of Pt and IrO_2 were calculated to be 13.0 and 2.2 nm using the Scherrer equation (Equation (1)) [34].

$$D = \frac{K\lambda}{\beta cos\theta} \tag{1}$$

where β is the full-width half maximum value, θ is the Bragg angle, K is the Scherrer constant (0.9), and λ is the wavelength of the incident X-ray. Nanosized electrode materials improve electrochemical activities due to their large surface area and high electrochemical surface area (ECSA) [51–53]. It is noted that according to recent studies [54,55], structural parameters (i.e., dislocation density and lattice strain) can be correlated with the particle size, affecting catalytic activities.
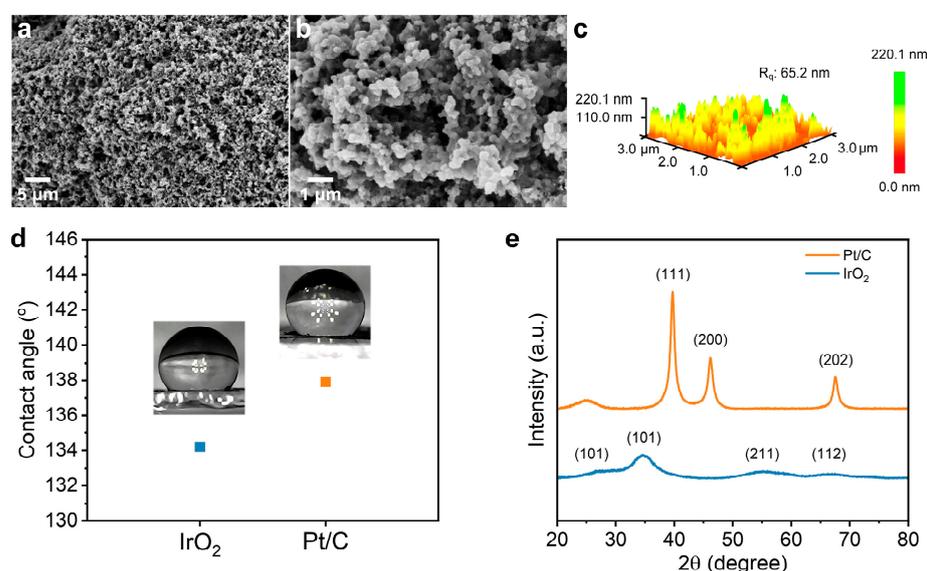

Figure 2. (**a**,**b**) SEM images at different magnifications and (**c**) AFM image of the Pt/C thin-film electrode on FTO. (**d**) Contact angles of IrO_2 and Pt/C on FTO. (**e**) XRD patterns of IrO_2 and Pt/C powders.

3.2. Electrochemical Properties of Thin-Film Electrodes

As described, the electrocatalyst inks of Pt/C and IrO_2 were spin-coated on FTO to evaluate the HER and OER activities in 0.1 M $HClO_4$. As mentioned, homogeneous and wettable electrode surfaces led to reproducible electrochemical measurements. Shown in Figure 3a are iR-compensated LSV measurements for the HER using the commercial and as-prepared Pt/C. Figure 3a demonstrates that the geometrical activity for Pt/C is close to that of commercial Pt/C, resulting in overpotentials of 71.3 and 73.8 mV at a current density of 10 mA/cm^2. As summarized in Figure 3b, their corresponding Tafel slopes are 39.9 and 40.9 mV/dec. Also, the overpotentials and the measuring environment are compared with those in the literature (Table S1 [56–64]). It is noted that most Pt exists with the oxidation state of Pt^0 under the (HER) conditions. Previous XPS studies demonstrated that active Pt nano-electrocatalysts can also exist as Pt^{2+} (PtO or Pt(OH)$_2$) and Pt^{4+} (PtO$_2$) [65,66]. Then, IrO_2 electrode materials were investigated under the same acidic conditions [67]. Vulcan carbon (XC-72) was used to prepare IrO_2 catalytic inks with 20 wt.% loading to enhance the conductivity. Figure 3c shows the OER polarization curves of IrO_2-based electrodes. The overpotentials of the as-prepared and commercial IrO_2 at 10 mA/cm^2 are 371.7 and 483.8 mV. Their corresponding Tafel slopes are 178.4 and

202.7 mV/dec (Figure 3d), demonstrating the superior OER performance of the as-prepared IrO_2 compared with that of commercial IrO_2 due to its hydrous amorphous structure of nano-sized metal oxide [34]. Similar to the Pt-based electrode materials, the recently reported values in the literature for IrO_2-based catalysts are summarized in Table S2 [68–77]. Then, as shown in Figure 3e, the overall water splitting was conducted using the as-prepared nano-sized Pt/C and IrO_2 with an overpotential of 0.44 V at 10 mA/cm^2.
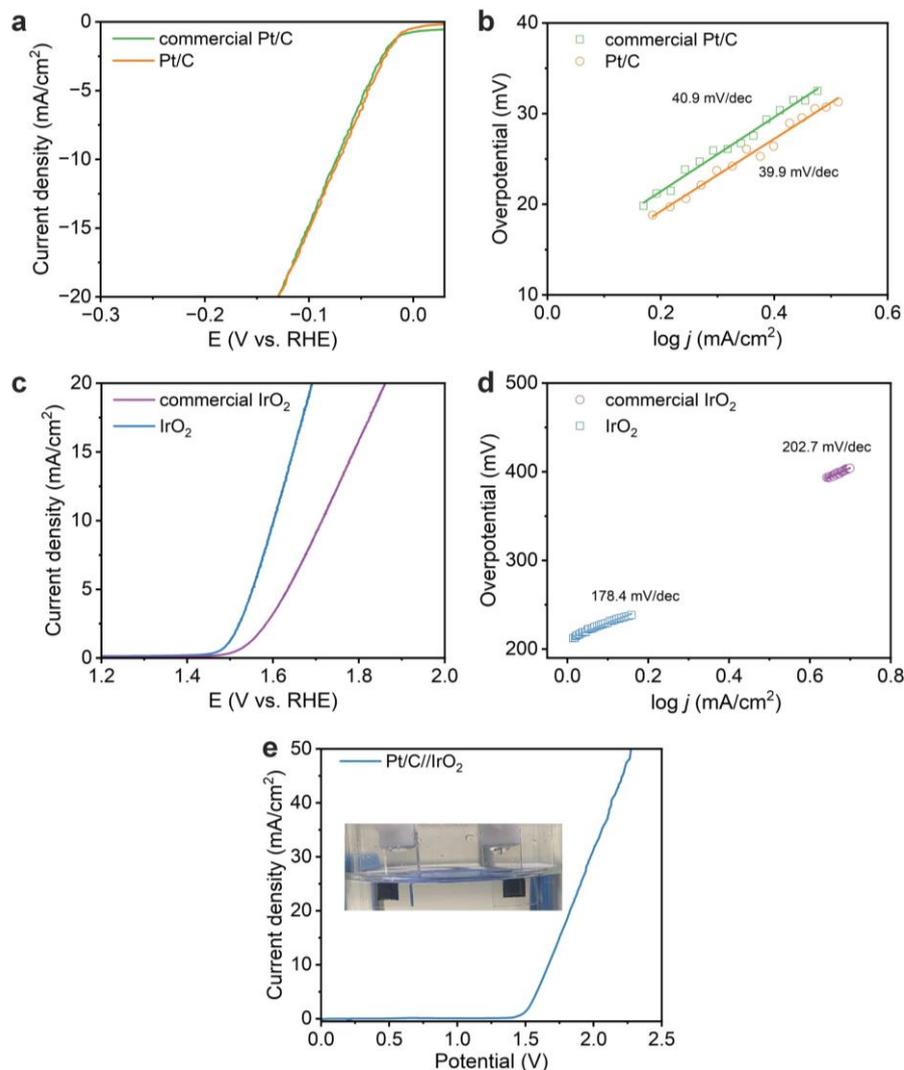
Figure 3. (**a**) HER polarization curves and (**b**) Tafel slopes of commercial and as-prepared Pt/C on FTO. (**c**) OER polarization curves and (**d**) Tafel slopes of commercial and as-prepared IrO_2 on FTO. (**e**) Polarization curve of overall water splitting of Pt/C versus IrO_2. The measurements were conducted in 0.1 M $HClO_4$ at a scan rate of 5 mV/s.

3.3. Kinetic Analysis of Oxygen Evolution on IrO_2 Using Electrochemical Impedance Spectroscopy

Electrochemical impedance spectroscopy (EIS) is one of the most powerful tools that characterizes the impedance response of electrode interfaces. To examine the reaction kinetic process, an accurate electrical equivalent circuit (EEC) is required for extracting the kinetic parameters and different overpotentials applied to the electrode. The rate-determining step (RDS) is studied by evaluating the electrode impedance response values during electrochemical reactions [78]. As is well known, IrO_2 and RuO_2 are the most efficient OER electrocatalysts under acid conditions. However, RuO_2 is easily degraded under harsh conditions [79]. Thus, as described in Figure 3c, in this study, IrO_2 was selected to conduct the kinetics analysis of oxygen evolution for exploring the capacitance and

impedance effects among adsorbate, electrolyte, and catalytic materials. A modified EEC, as shown in Figure 4a, is applied to explain multiple adsorbed intermediates on electrode surfaces, and the EEC model comprises two RC circuits based on the Randles circuit [26,80]. In this study, we used the OER process under acidic conditions, where OH_{ad} and O_{ad} are the intermediates adsorbed on the IrO_2 electrode surface [26,28]. The EEC contains an electrolyte resistance (R_s) in series with the capacitance of the electrode double layer (C_{dl}) in parallel with a pair of the impedances of the intermediates generated during the adsorption process, which involves an adsorption resistance (R_{ads}) and an adsorption capacitance (C_{ads}) in series with the resistance of the charge transfer process (R_{ct}), including an electron transfer process both within the electrode and at the electrode/electrolyte interface. The EEC model can also be presented as $R_s + C_{dl}/(R_{ct} + C_{ads}/R_{ads})$, where C_{ads}/R_{ads} is the impedance of the intermediate species on the IrO_2 electrode (i.e., oxygen species in this study) for modeling charge relaxation [81]. Figure 4a shows Nyquist plots for IrO_2 at different potentials, revealing the domain Faradaic resistance. As summarized in Table 1, R_{ads} values significantly decrease with increasing overpotential, which originates from the accelerated diffusion and transfer of the intermediates adsorbed on the electrode surface. The impedance resistance arc decreases [26] as the overpotential increases. Accordingly, the relaxation of the adsorbed intermediates is generally considered the RDS of OER processes [26,82]. Intermediates adsorbed on electrode surfaces may not be the same using different electrocatalysts. The RDS can be effectively investigated by evaluating the significant capacitance associated with surface intermediates [82,83]. The relationship between the current density (*j*) and the electrode potential is precisely expressed by the Bulter–Volmer equation. According to a previous study [26], the reaction admittance (Y) describes how freely a circuit allows a current flow. *j* is the current density of the electrode, j_0 is the exchange current density, and T is the temperature.

$$Y = (\partial j / \partial E)_T \tag{2}$$

The total reaction resistance of OER, then, is defined as $R = Y^{-1}$ [28]. It can be modified to a Tafel-like linear relationship [84].

$$log(R^{-1}) = log(R^{*-1}) + \alpha_{apa} F(E - E_0)/2.303 R_g T \tag{3}$$

$$R^* = R_g T / \alpha_{apa} F j_{0(apa)} \tag{4}$$

$$\alpha_{apa} = \frac{2RTb}{4F} \tag{5}$$

where F is the Faraday constant, α_{apa} is the apparent charge transfer coefficient of the rate-determining step, R_g is the gas constant, and $E - E_0$ is the overpotential. Accordingly, the charge transfer coefficient (α_{apa}) is accurately calculated from its slope, while the exchange current density (j_0) can be obtained through its intercept. Then, the crucial OER kinetic parameters are extracted using the kinetic model. Experimentally, R_{ads} values were measured as a function of potentials for the OER kinetic study using the EIS approach (Figure 4b) [26]. The EIS study produced the charge transfer coefficient of IrO_2 (0.10) by applying the EEC shown in Figure 4a. We then obtained the exchange current density of IrO_2 (6.7×10^{-2} mA/cm^2), which agrees with that from the Tafel slope method (5.1×10^{-2} mA/cm^2). The kinetic method determines the exchange current density using resistance (R_{ads}) (Figure 4c) to describe the OER mechanism compared with the Tafel slope analysis [26]. Figure 4d,e indicate the Bode plots of the IrO_2 electrode prepared on FTO measured at cell densities 2, 4, 6, 8, and 10 mA/cm^2. From the Bode phase plot, it can be noticed that there is a stable peak in the high-frequency (HF) region and a peak change in the low-frequency (LF) region, followed by applied voltage (current density) increases. The peak in the HF region can be attributed to the characteristic frequency of the material ($10^{3.28}$ Hz for IrO_2), which is defined by the frequency of the highest impedance value of

the imaginary part of the semicircle in an HF region [85]. Furthermore, the Bode phase plot in the LF region exhibits a peak frequency shifted towards the HF region as the applied current density increases, which can be explained by the faster OER kinetics [86]. To further understand the time constant of high current density in two semicircles of time and the impedance distribution, a distribution of relaxation times (DRT) analysis [87] was performed using the impedance data measured at different current densities [87–89] by deconvoluting the EIS data. Figure 5a,b show that IrO$_2$ has stable impedance values at a time constant (τ) of 1.0×10^{-5} s in the HF region. This can be interpreted as a charge transfer process at the electrode material/electrolyte interface with the contact impedance [90]. Several peak values between 1.0×10^{-4} s and 1.0×10^{-2} s can be observed due to the OER process. A time constant of 1×10^{-1} s in the LF region decreases with the increase in current density and with the decrease in the time constant because of the capacitance response of the electrode surface and O-intermediate coverage on the catalytic active sites. Meanwhile, as the applied overpotential increases, the time constant changes because of the accelerated diffusion and transfer process of the O intermediate [26], which is consistent with the results of the Nyquist plot in the large semicircle in the LF region and the characteristic frequency of the Bode phase plot [91]. We plan to perform more systematic studies for designing novel high-performance OER electrode materials using EIS-based kinetic studies, which align with the Tafel slope analysis.
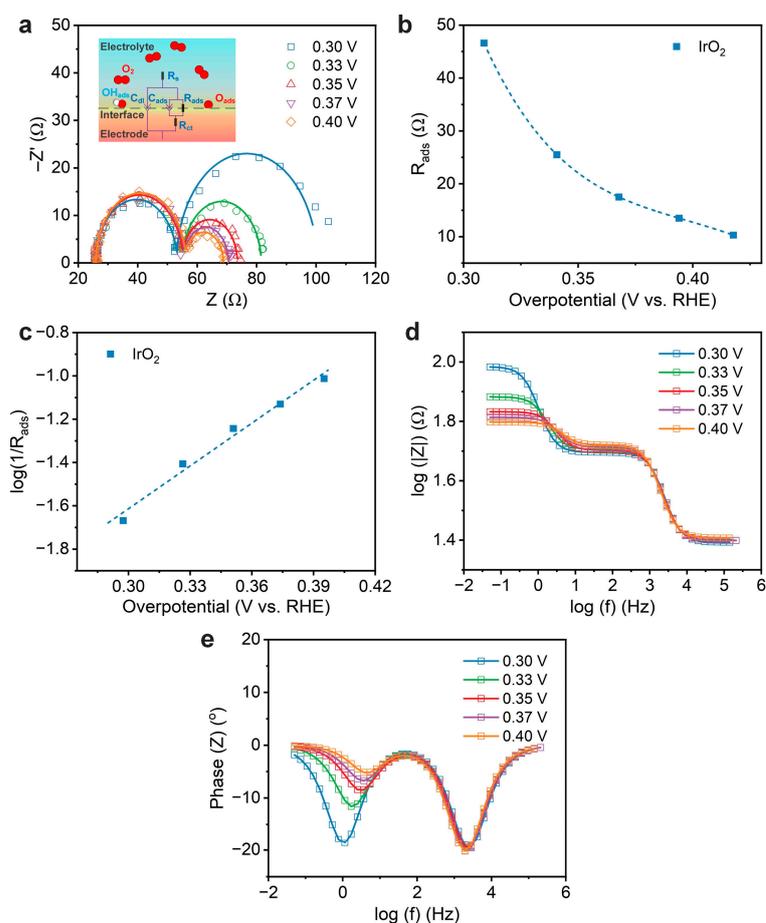
Figure 4. (**a**) Nyquist plots, (**b**) overpotential-dependent R$_{ads}$ variation in the kinetic analysis using EIS, and (**c**) log(1/R$_{ads}$) as a function of the overpotentials of IrO$_2$ under OER conditions. An illustration of the electrical equivalent circuit (EEC) model used for the EIS analyses is shown [26]. Bode plots of (**d**) impedance magnitude versus frequency and (**e**) phase angle versus frequency.

Table 1. EIS fitting parameters of IrO_2 nano-electrocatalysts deposited on FTO.

Overpotential (V) [1]	R_s (Ω)	$C_{dl} \times 10^{-6}$ (F)	R_{ct} (Ω)	$C_{ads} \times 10^{-3}$ (F)	R_{ads} (Ω)	$\log(1/R_{ads})$
0.30	24.7	4.14	25.0	4.53	46.6	−1.67
0.33	25.1	4.02	25.7	4.18	25.5	−1.41
0.35	25.2	3.75	25.3	3.41	17.5	−1.24
0.37	25.4	4.19	25.7	3.77	13.5	−1.13
0.40	25.5	4.28	26.9	3.86	10.3	−1.01

[1] V versus RHE.
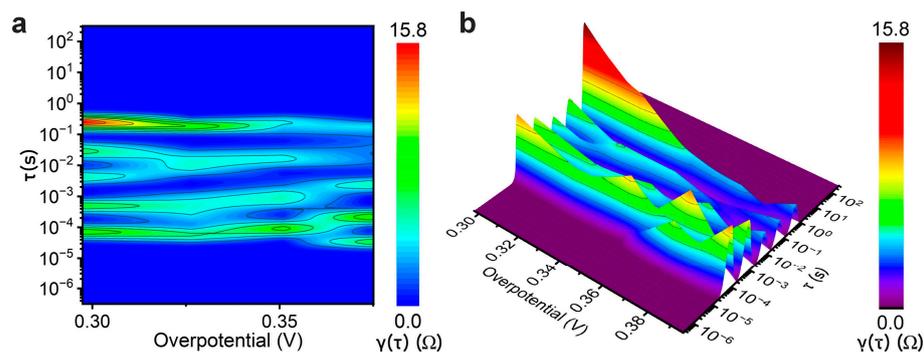
Figure 5. The (**a**) 2D and (**b**) 3D DRT plots of the IrO_2 electrode on FTO.

4. Conclusions

Nanoscale Pt/C and IrO_2 electrocatalysts were synthesized, and their thin-film electrodes were fabricated on FTO using the spin-coating method to validate their electrochemical efficiencies in water splitting. The electrocatalytic activities of Pt/C and IrO_2 on FTO were close to those of commercial Pt/C and superior to those of commercial IrO_2, exhibiting improved overall water splitting performance. Furthermore, an OER kinetics analysis of the IrO_2 nano-electrocatalysts was conducted based on the EEC model using EIS measurements. It was observed that the exchange current density of the IrO_2 electrode was in good agreement with that of the Tafel slope method (6.7×10^{-2} mA/cm^2 versus 5.1×10^{-2} mA/cm^2), indicating the validity of the microkinetic models used for the kinetic analysis. Systematic in situ characterization of the OER electrocatalysts using Fourier-transform infrared spectroscopy (FTIR) and X-ray photoelectron spectroscopy (XPS) can improve kinetics analyses [54]. In addition, advanced surface morphological and elemental analyses using high-resolution SEM and TEM may provide a better understanding of active sites in kinetic analysis. The EIS-based kinetic method could be applied to propose novel and highly active electrode materials for electrocatalytic and photoelectrocatalytic water electrolysis and novel energy materials.

Author Contributions: Conceptualization, Y.C.; methodology, Y.C.; investigation, Y.-W.L., Y.-S.L., C.-W.C. and T.-H.Y.; data curation, Y.-W.L., Y.-S.L., C.-W.C. and Y.-T.L.; visualization, Y.-W.L. and L.-C.H.; writing—original draft preparation, Y.-W.L., Y.-S.L. and C.-W.C.; writing—review and editing, D.K.P., C.C. and Y.C.; supervision, Y.C.; project administration, Y.C. All authors have read and agreed to the published version of the manuscript.

Institutional Review Board Statement: Not applicable.

Informed Consent Statement: Not applicable.

References

1. Kakoulaki, G.; Kougias, I.; Taylor, N.; Dolci, F.; Moya, J.; Jäger-Waldau, A. Green hydrogen in Europe-A regional assessment: Substituting existing production with electrolysis powered by renewables. *Energy Convers. Manag.* **2021**, *228*, 113649. [CrossRef]
2. Morales-Guio, C.G.; Stern, L.-A.; Hu, X. Nanostructured hydrotreating catalysts for electrochemical hydrogen evolution. *Chem. Soc. Rev.* **2014**, *43*, 6555–6569. [CrossRef] [PubMed]
3. Cheng, C.-C.; Yeh, Y.-X.; Ting, Y.-C.; Lin, S.-H.; Sasaki, K.; Choi, Y.; Lu, S.-Y. Modulation of the coordination environment enhances the electrocatalytic efficiency of Mo single atoms toward water splitting. *J. Mater. Chem. A* **2022**, *10*, 8784–8797. [CrossRef]
4. Vos, J.G.; Wezendonk, T.A.; Jeremiasse, A.W.; Koper, M.T. MnO_x/IrO_x as selective oxygen evolution electrocatalyst in acidic chloride solution. *J. Am. Chem. Soc.* **2018**, *140*, 10270–10281. [CrossRef] [PubMed]
5. Tee, S.Y.; Win, K.Y.; Teo, W.S.; Koh, L.D.; Liu, S.; Teng, C.P.; Han, M.Y. Recent progress in energy-driven water splitting. *Adv. Sci.* **2017**, *4*, 1600337. [CrossRef]
6. Mehrpooya, M.; Ghorbani, B.; Ekrataleshian, A.; Mousavi, S.A. Investigation of hydrogen production by sulfur-iodine thermochemical water splitting cycle using renewable energy source. *Int. J. Energy Res.* **2021**, *45*, 14845–14869. [CrossRef]
7. Huang, C.L.; Sasaki, K.; Senthil Raja, D.; Hsieh, C.T.; Wu, Y.J.; Su, J.T.; Cheng, C.C.; Cheng, P.Y.; Lin, S.H.; Choi, Y. Twinning enhances efficiencies of metallic catalysts toward electrolytic water splitting. *Adv. Energy Mater.* **2021**, *11*, 2101827. [CrossRef]
8. Liu, J.; Chen, C.; Wu, H.; Cheng, J. Kinetics and oxidation pathways of Fe^{3+}-catalyzed carbon-assisted water electrolysis for hydrogen production. *Int. J. Hydrogen Energy* **2022**, *47*, 20432–20447. [CrossRef]
9. Liu, Y.; Zhou, D.; Deng, T.; He, G.; Chen, A.; Sun, X.; Yang, Y.; Miao, P. Research progress of oxygen evolution reaction catalysts for electrochemical water splitting. *ChemSusChem* **2021**, *14*, 5359–5383. [CrossRef]
10. Singh, M.R.; Clark, E.L.; Bell, A.T. Effects of electrolyte, catalyst, and membrane composition and operating conditions on the performance of solar-driven electrochemical reduction of carbon dioxide. *Phys. Chem. Chem. Phys.* **2015**, *17*, 18924–18936. [CrossRef]
11. You, B.; Sun, Y. Innovative strategies for electrocatalytic water splitting. *Accounts Chem. Res.* **2018**, *51*, 1571–1580. [CrossRef]
12. Raja, D.S.; Huang, C.-L.; Chen, Y.-A.; Choi, Y.; Lu, S.-Y. Composition-balanced trimetallic MOFs as ultra-efficient electrocatalysts for oxygen evolution reaction at high current densities. *Appl. Catal. B* **2020**, *279*, 119375. [CrossRef]
13. Wu, Z.-Y.; Chen, F.-Y.; Li, B.; Yu, S.-W.; Finfrock, Y.Z.; Meira, D.M.; Yan, Q.-Q.; Zhu, P.; Chen, M.-X.; Song, T.-W.; et al. Non-iridium-based electrocatalyst for durable acidic oxygen evolution reaction in proton exchange membrane water electrolysis. *Nat. Mater.* **2023**, *22*, 100–108. [CrossRef] [PubMed]
14. Chen, L.-W.; Liang, H.-W. Ir-based bifunctional electrocatalysts for overall water splitting. *Catal. Sci. Technol.* **2021**, *11*, 4673–4689. [CrossRef]
15. Fu, L.; Zeng, X.; Cheng, G.; Luo, W. IrCo nanodendrite as an efficient bifunctional electrocatalyst for overall water splitting under acidic conditions. *ACS Appl. Mater. Interfaces* **2018**, *10*, 24993–24998. [CrossRef] [PubMed]
16. Fu, L.; Hu, X.; Li, Y.; Cheng, G.; Luo, W. IrW nanobranches as an advanced electrocatalyst for pH-universal overall water splitting. *Nanoscale* **2019**, *11*, 8898–8905. [CrossRef] [PubMed]
17. Liu, M.; Liu, S.; Mao, Q.; Yin, S.; Wang, Z.; Xu, Y.; Li, X.; Wang, L.; Wang, H. Ultrafine ruthenium-iridium-tellurium nanotubes for boosting overall water splitting in acidic media. *J. Mater. Chem. A* **2022**, *10*, 2021–2026. [CrossRef]
18. Yang, N.; Tian, S.; Feng, Y.; Hu, Z.; Liu, H.; Tian, X.; Xu, L.; Hu, C.; Yang, J. Introducing High-Valence Iridium Single Atoms into Bimetal Phosphides toward High-Efficiency Oxygen Evolution and Overall Water Splitting. *Small* **2023**, *19*, 2207253. [CrossRef]
19. Yang, C.; Zhang, X.; An, Q.; Liu, M.; Zhou, W.; Li, Y.; Hu, F.; Liu, Q.; Su, H. Dynamically-evolved surface heterojunction in iridium nanocrystals boosting acidic oxygen evolution and overall water splitting. *J. Energy Chem.* **2023**, *78*, 374–380. [CrossRef]
20. Wang, Q.; Xu, C.-Q.; Liu, W.; Hung, S.-F.; Bin Yang, H.; Gao, J.; Cai, W.; Chen, H.M.; Li, J.; Liu, B. Coordination engineering of iridium nanocluster bifunctional electrocatalyst for highly efficient and pH-universal overall water splitting. *Nat. Commun.* **2020**, *11*, 4246. [CrossRef]
21. Wan, C.; Duan, X.; Huang, Y. Molecular Design of Single-Atom Catalysts for Oxygen Reduction Reaction. *Adv. Energy Mater.* **2020**, *10*, 1903815. [CrossRef]
22. Liu, B.-J.; Yin, T.-H.; Lin, Y.-W.; Chang, C.-W.; Yu, H.-C.; Lim, Y.; Lee, H.; Choi, C.; Tsai, M.-K.; Choi, Y. A Cost-Effective, Nanoporous, High-Entropy Oxide Electrode for Electrocatalytic Water Splitting. *Coatings* **2023**, *13*, 1461. [CrossRef]
23. Yu, S.; Li, K.; Wang, W.; Xie, Z.; Ding, L.; Kang, Z.; Wrubel, J.; Ma, Z.; Bender, G.; Yu, H.; et al. Tuning Catalyst Activation and Utilization Via Controlled Electrode Patterning for Low-Loading and High-Efficiency Water Electrolyzers. *Small* **2022**, *18*, 2107745. [CrossRef]
24. Chen, S.; Li, X.; Kao, C.-W.; Luo, T.; Chen, K.; Fu, J.; Ma, C.; Li, H.; Li, M.; Chan, T.-S.; et al. Unveiling the Proton-Feeding Effect in Sulfur-Doped Fe-N-C Single-Atom Catalyst for Enhanced CO_2 Electroreduction. *Angew. Chem.-Int. Edit.* **2022**, *61*, e202206233. [CrossRef] [PubMed]

25. Zhai, P.; Wang, C.; Zhao, Y.; Zhang, Y.; Gao, J.; Sun, L.; Hou, J. Regulating electronic states of nitride/hydroxide to accelerate kinetics for oxygen evolution at large current density. *Nat. Commun.* **2023**, *14*, 1873. [CrossRef] [PubMed]

26. Lu, Y.; Wang, W.; Xie, F. Investigation of oxygen evolution reaction kinetic process and kinetic parameters on iridium electrode by electrochemistry impedance spectroscopy analysis. *J. Electroanal. Chem.* **2020**, *871*, 114281. [CrossRef]

27. Schröder, J.; Mints, V.A.; Bornet, A.; Berner, E.; Fathi Tovini, M.; Quinson, J.; Wiberg, G.K.H.; Bizzotto, F.; El-Sayed, H.A.; Arenz, M. The Gas Diffusion Electrode Setup as Straightforward Testing Device for Proton Exchange Membrane Water Electrolyzer Catalysts. *JACS Au* **2021**, *1*, 247–251. [CrossRef]

28. Costa, F.R.; Franco, D.V.; Da Silva, L.M. Electrochemical impedance spectroscopy study of the oxygen evolution reaction on a gas-evolving anode composed of lead dioxide microfibers. *Electrochim. Acta* **2013**, *90*, 332–343. [CrossRef]

29. Benck, J.D.; Pinaud, B.A.; Gorlin, Y.; Jaramillo, T.F. Substrate selection for fundamental studies of electrocatalysts and photoelectrodes: Inert potential windows in acidic, neutral, and basic electrolyte. *PLoS ONE* **2014**, *9*, e107942. [CrossRef]

30. Cheng, P.-Y.; Ting, Y.-C.; Cheng, C.-C.; Raja, D.S.; Lin, S.-H.; Yeh, Y.-X.; Su, J.-T.; Lu, S.-Y. Nitrogen-doped carbon armored Cobalt oxide hollow nanocubes electrochemically anchored on fluorine-doped tin oxide substrate for acidic oxygen evolution reaction. *J. Colloid Interface Sci.* **2022**, *623*, 327–336. [CrossRef]

31. He, F.; Zhou, Y.; Hu, T.; Xu, Y.; Hou, M.; Zhu, F.; Liu, D.; Zhang, H.; Xu, K.; Liu, M.; et al. An Efficient High-Entropy Perovskite-Type Air Electrode for Reversible Oxygen Reduction and Water Splitting in Protonic Ceramic Cells. *Adv. Mater.* **2023**, *35*, 2209469. [CrossRef]

32. Giesbrecht, P.K.; Freund, M.S. Investigation of Water Oxidation at IrO_2 Electrodes in Nafion-Based Membrane Electrode Assemblies Using Impedance Spectroscopy and Distribution of Relaxation Times Analysis. *J. Phys. Chem. C* **2022**, *126*, 17844–17861. [CrossRef]

33. Song, L.; Cai, Y.; Liu, Y.; Zhao, X.; Kuttiyiel, K.A.; Marinkovic, N.; Frenkel, A.I.; Kongkanand, A.; Choi, Y.; Adzic, R.R. One-Step Facile Synthesis of High-Activity Nitrogen-Doped PtNiN Oxygen Reduction Catalyst. *ACS Appl. Energy Mater.* **2022**, *5*, 5245–5255. [CrossRef]

34. Felix, C.; Bladergroen, B.J.; Linkov, V.; Pollet, B.G.; Pasupathi, S. Ex-situ electrochemical characterization of IrO_2 synthesized by a modified Adams fusion method for the oxygen evolution reaction. *Catalysts* **2019**, *9*, 318. [CrossRef]

35. Puthiyapura, V.K.; Mamlouk, M.; Pasupathi, S.; Pollet, B.G.; Scott, K. Physical and electrochemical evaluation of ATO supported IrO_2 catalyst for proton exchange membrane water electrolyser. *J. Power Sources* **2014**, *269*, 451–460. [CrossRef]

36. Jeong, Y.J.; Seo, D.H.; Baek, J.H.; Kang, M.J.; Kim, B.N.; Kim, S.K.; Zheng, X.; Cho, I.S. Crystal Reconstruction of Mo:$BiVO_4$: Improved Charge Transport for Efficient Solar Water Splitting. *Adv. Funct. Mater.* **2022**, *32*, 2208196. [CrossRef]

37. Bi, W.; Fuller, T.F. Modeling of PEM fuel cell Pt/C catalyst degradation. *J. Power Sources* **2008**, *178*, 188–196. [CrossRef]

38. Li, P.; Wang, Y.; Du, X.; Zhang, X. Promoted electrocatalytic water splitting by regulating the concentration of oxygen vacancies. *Int. J. Hydrogen Energy* **2023**, *48*, 34783–34793. [CrossRef]

39. Shetty, A.R.; Hegde, A.C. Effect of TiO_2 on electrocatalytic behavior of Ni-Mo alloy coating for hydrogen energy. *Mater. Sci. Energy Technol.* **2018**, *1*, 97–105. [CrossRef]

40. Kim, B.K.; Kim, M.J.; Kim, J.J. Impact of Surface Hydrophilicity on Electrochemical Water Splitting. *ACS Appl. Mater. Interfaces* **2021**, *13*, 11940–11947. [CrossRef]

41. Wang, Z.; Liu, G.; Ding, C.; Chen, Z.; Zhang, F.; Shi, J.; Li, C. Synergetic Effect of Conjugated $Ni(OH)_2$/IrO_2 Cocatalyst on Titanium-Doped Hematite Photoanode for Solar Water Splitting. *J. Phys. Chem. C* **2015**, *119*, 19607–19612. [CrossRef]

42. Hyun Oh, J.; Ho Han, G.; Kim, J.; Eun Lee, J.; Kim, H.; Kyung Kang, S.; Kim, H.; Wooh, S.; Soo Lee, P.; Won Jang, H.; et al. Self-supported electrodes to enhance mass transfer for high-performance anion exchange membrane water electrolyzer. *Chem. Eng. J.* **2023**, *460*, 141727. [CrossRef]

43. Wang, Y.; Xue, Y.; Zhang, C. Rational Surface and Interfacial Engineering of IrO_2/TiO_2 Nanosheet Arrays toward High-Performance Chlorine Evolution Electrocatalysis and Practical Environmental Remediation. *Small* **2021**, *17*, 2006587. [CrossRef]

44. Li, H.; Pan, Y.; Wu, L.; He, R.; Qin, Z.; Luo, S.; Yang, L.; Zeng, J. Highly active and stable IrO_2 and IrO_2-Ta_2O_5 catalysts for oxygen evolution reaction. *Int. J. Hydrogen Energy* **2023**, *48*, 26021–26031. [CrossRef]

45. Uzunoglu, A.; Ipekci, H.H. The use of CeO_2-modified Pt/C catalyst inks for the construction of high-performance enzyme-free H_2O_2 sensors. *J. Electroanal. Chem.* **2019**, *848*, 113302. [CrossRef]

46. Sriring, N.; Tantavichet, N.; Pruksathorn, K. Preparation of Pt/C catalysts by electroless deposition for proton exchange membrane fuel cells. *Korean J. Chem. Eng.* **2010**, *27*, 439–445. [CrossRef]

47. Singh, A.; Miyabayashi, K. Novel continuous flow synthesis of Pt NPs with narrow size distribution for Pt@ carbon catalysts. *RSC Adv.* **2020**, *10*, 362–366. [CrossRef]

48. Huy, H.A.; Van Man, T.; Tai, H.T. Preparation and characterization of high-dispersed Pt/C nano-electrocatalysts for fuel cell applications. *Vietnam J. Sci. Technol.* **2016**, *54*, 472–482. [CrossRef]

49. Zheng, H.-B.; An, L.; Zheng, Y.; Qu, C.; Fang, Y.; Liu, Q.; Dang, D. Tuning the catalytic activity of Ir@Pt nanoparticles through controlling Ir core size on cathode performance for PEM fuel cell application. *Front. Chem.* **2018**, *6*, 299. [CrossRef]

50. Qin, B.; Yu, H.; Chi, J.; Jia, J.; Gao, X.; Yao, D.; Yi, B.; Shao, Z. A novel Ir/CeO_2-C nanoparticle electrocatalyst for the hydrogen oxidation reaction of alkaline anion exchange membrane fuel cells. *RSC Adv.* **2017**, *7*, 31574–31581. [CrossRef]

51. Zhao, X.; Chen, M.; Zhou, Y.; Zhang, H.; Hu, G. Fluorinated MXenes accelerate the hydrogen evolution activity of in situ induced snowflake-like nano-Pt. *J. Mater. Chem. A* **2023**, *11*, 5830–5840. [CrossRef]

52. Zeng, Z.; Küspert, S.; Balaghi, S.E.; Hussein, H.E.; Ortlieb, N.; Knäbbeler-Buß, M.; Hügenell, P.; Pollitt, S.; Hug, N.; Melke, J. Ultrahigh Mass Activity Pt Entities Consisting of Pt Single atoms, Clusters, and Nanoparticles for Improved Hydrogen Evolution Reaction. *Small* **2023**, *19*, 2205885. [CrossRef]

53. Mendoza-Pérez, R.; Guisbiers, G. Bimetallic Pt-Pd nano-catalyst: Size, shape and composition matter. *Nanotechnology* **2019**, *30*, 305702. [CrossRef]

54. Saeed, U.; Jilani, A.; Iqbal, J.; Al-Turaif, H. Reduced graphene oxide-assisted graphitic carbon nitride@ZnO rods for enhanced physical and photocatalytic degradation. *Inorg. Chem. Commun.* **2022**, *142*, 109623. [CrossRef]

55. Jilani, A.; Hussain, S.Z.; Ansari, M.O.; Kumar, R.; Dustgeer, M.R.; Othman, M.H.D.; Barakat, M.A.; Melaibari, A.A. Facile synthesis of silver decorated reduced graphene oxide@zinc oxide as ternary nanocomposite: An efficient photocatalyst for the enhanced degradation of organic dye under UV-visible light. *J. Mater. Sci.* **2021**, *56*, 7434–7450. [CrossRef]

56. Yu, B.; Liu, J.-H.; Guo, S.; Huang, G.; Zhang, S.; Chen, S.; Li, X.; Wang, Y.; Lv, L.-P. Densely populated tiny RuO_2 crystallites supported by hierarchically porous carbon for full acidic water splitting. *Mater. Horizons* **2023**, *10*, 4589–4596. [CrossRef]

57. Shi, J.; Kao, C.-w.; Lan, J.; Jiang, K.; Peng, M.; Luo, M.; Lu, Y.-R.; Zhang, S.; Tan, Y. Nanoporous PdIr alloy for high-efficiency and durable water splitting in acidic media. *J. Mater. Chem. A* **2023**, *11*, 11526–11533. [CrossRef]

58. Xie, Y.; Chang, C.; Luo, F.; Yang, Z. Modulation in the d Band of Ir by Core-Shell Construction for Robust Water Splitting Electrocatalysts in Acid. *ACS Appl. Mater. Interfaces* **2023**, *15*, 20081–20088. [CrossRef]

59. Shao, X.; Liang, M.; Kim, M.G.; Ajmal, S.; Kumar, A.; Liu, X.; Jung, H.S.; Jin, H.; Cao, F.; Yu, J.; et al. Density-Controlled Metal Nanocluster with Modulated Surface for pH-Universal and Robust Water Splitting. *Adv. Funct. Mater.* **2023**, *33*, 2211192. [CrossRef]

60. Liu, Z.; Liu, Y.; He, H.; Shao, H.; Zhang, Y.; Li, J.; Cai, W. Valence regulation of Ru/Mo_2C heterojunction for efficient acidic overall water splitting. *Electrochim. Acta* **2023**, *443*, 141920. [CrossRef]

61. Khamgaonkar, S.; Chen, Q.; Musselman, K.; Maheshwari, V. Stable perovskite photocathodes for efficient hydrogen evolution in acidic and basic conditions. *J. Mater. Chem. A* **2023**, *11*, 20079–20088. [CrossRef]

62. Kuang, P.; Wang, Y.; Zhu, B.; Xia, F.; Tung, C.-W.; Wu, J.; Chen, H.M.; Yu, J. Pt Single Atoms Supported on N-Doped Mesoporous Hollow Carbon Spheres with Enhanced Electrocatalytic H_2-Evolution Activity. *Adv. Mater.* **2021**, *33*, 2008599. [CrossRef]

63. Kaneva, M.V.; Gulina, L.B.; Tolstoy, V.P. Pt nanoparticles synthesized by successive ionic layers deposition method and their electrocatalytic properties in hydrogen evolution reaction during water splitting in the acidic medium. *J. Alloys Compd.* **2022**, *901*, 163640. [CrossRef]

64. Ge, Y.; Wang, X.; Chen, B.; Huang, Z.; Shi, Z.; Huang, B.; Liu, J.; Wang, G.; Chen, Y.; Li, L.; et al. Preparation of fcc-2H-fcc Heterophase Pd@Ir Nanostructures for High-Performance Electrochemical Hydrogen Evolution. *Adv. Mater.* **2022**, *34*, 2107399. [CrossRef]

65. Huang, Y.; Ma, D.; Liu, W.; Xia, D.; Hu, L.; Yang, J.; Liao, P.; He, C. Enhanced Catalytic Ozonation for Eliminating CH_3SH via Graphene-Supported Positively Charged Atomic Pt Undergoing Pt^{2+}/Pt^{4+} Redox Cycle. *Environ. Sci. Technol.* **2021**, *55*, 16723–16734. [CrossRef] [PubMed]

66. Prabhuram, J.; Wang, X.; Hui, C.L.; Hsing, I.M. Synthesis and Characterization of Surfactant-Stabilized Pt/C Nanocatalysts for Fuel Cell Applications. *J. Phys. Chem. B* **2003**, *107*, 11057–11064. [CrossRef]

67. Zaman, W.Q.; Sun, W.; Tariq, M.; Zhou, Z.; Farooq, U.; Abbas, Z.; Cao, L.; Yang, J. Iridium substitution in nickel cobaltite renders high mass specific OER activity and durability in acidic media. *Appl. Catal. B* **2019**, *244*, 295–302. [CrossRef]

68. Wang, Y.; Guo, X.; Wang, X.; Huang, J.; Yin, L.; Zhu, W.; Zhuang, Z. Construction of Steady-Active Self-supported Porous Ir-based Electrocatalysts for Oxygen Evolution Reaction. *Chem. Commun.* **2023**, *59*, 1813–1816. [CrossRef]

69. Zheng, Y.; Ye, Z.; Peng, X.; Zhuang, S.; Li, D.; Jin, Z. Cobalt vacancy-originated TiMnCoCN compounds with a self-adjusting ability for the high-efficiency acidic oxygen evolution reaction. *J. Colloid Interface Sci.* **2023**, *652*, 164–173. [CrossRef]

70. Raja, D.S.; Cheng, P.-Y.; Cheng, C.-C.; Chang, S.-Q.; Huang, C.-L.; Lu, S.-Y. In-situ grown metal-organic framework-derived carbon-coated Fe-doped cobalt oxide nanocomposite on fluorine-doped tin oxide glass for acidic oxygen evolution reaction. *Appl. Catal. B* **2022**, *303*, 120899. [CrossRef]

71. Dang, Q.; Lin, H.; Fan, Z.; Ma, L.; Shao, Q.; Ji, Y.; Zheng, F.; Geng, S.; Yang, S.-Z.; Kong, N.; et al. Iridium metallene oxide for acidic oxygen evolution catalysis. *Nat. Commun.* **2021**, *12*, 6007. [CrossRef] [PubMed]

72. Li, Q.; Li, J.; Xu, J.; Zhang, N.; Li, Y.; Liu, L.; Pan, D.; Wang, Z.; Deepak, F.L. Ultrafine-grained porous Ir-based catalysts for high-performance overall water splitting in acidic media. *ACS Appl. Energy Mater.* **2020**, *3*, 3736–3744. [CrossRef]

73. Cai, C.; Han, S.; Tang, Y. Engineering oxygen vacancies on dendrite-like IrO_2 for the oxygen evolution reaction in acidic solution. *Sustain. Energy Fuels* **2020**, *4*, 2462–2468. [CrossRef]

74. Chen, X.; Xu, M.; Li, S.; Li, C.; Sun, X.; Mu, S.; Yu, J. Ultrafine IrNi Bimetals Encapsulated in Zeolitic Imidazolate Frameworks-Derived Porous N-Doped Carbon for Boosting Oxygen Evolution in Both Alkaline and Acidic Electrolytes. *Adv. Mater. Interfaces* **2020**, *7*, 2001145. [CrossRef]

75. Yao, Q.; Huang, B.; Xu, Y.; Li, L.; Shao, Q.; Huang, X. A chemical etching strategy to improve and stabilize RuO_2-based nanoassemblies for acidic oxygen evolution. *Nano Energy* **2021**, *84*, 105909. [CrossRef]

76. Wang, Y.; Zhang, L.; Yin, K.; Zhang, J.; Gao, H.; Liu, N.; Peng, Z.; Zhang, Z. Nanoporous Iridium-Based Alloy Nanowires as Highly Efficient Electrocatalysts Toward Acidic Oxygen Evolution Reaction. *ACS Appl. Mater. Interfaces* **2019**, *11*, 39728–39736. [CrossRef]

77. Li, G.; Li, S.; Xiao, M.; Ge, J.; Liu, C.; Xing, W. Nanoporous IrO_2 catalyst with enhanced activity and durability for water oxidation owing to its micro/mesoporous structure. *Nanoscale* **2017**, *9*, 9291–9298. [CrossRef]

78. Jin, C.; Lu, F.; Cao, X.; Yang, Z.; Yang, R. Facile synthesis and excellent electrochemical properties of $NiCo_2O_4$ spinel nanowire arrays as a bifunctional catalyst for the oxygen reduction and evolution reaction. *J. Mater. Chem. A* **2013**, *1*, 12170–12177. [CrossRef]

79. Bizzotto, F.; Quinson, J.; Zana, A.; Kirkensgaard, J.J.; Dworzak, A.; Oezaslan, M.; Arenz, M. Ir nanoparticles with ultrahigh dispersion as oxygen evolution reaction (OER) catalysts: Synthesis and activity benchmarking. *Catal. Sci. Technol.* **2019**, *9*, 6345–6356. [CrossRef]

80. Bredar, A.R.C.; Chown, A.L.; Burton, A.R.; Farnum, B.H. Electrochemical Impedance Spectroscopy of Metal Oxide Electrodes for Energy Applications. *ACS Appl. Energy Mater.* **2020**, *3*, 66–98. [CrossRef]

81. Lyons, M.E.; Brandon, M.P. The significance of electrochemical impedance spectra recorded during active oxygen evolution for oxide covered Ni, Co and Fe electrodes in alkaline solution. *J. Electroanal. Chem.* **2009**, *631*, 62–70. [CrossRef]

82. García-Osorio, D.A.; Jaimes, R.; Vazquez-Arenas, J.; Lara, R.H.; Alvarez-Ramirez, J. The Kinetic Parameters of the Oxygen Evolution Reaction (OER) Calculated on Inactive Anodes via EIS Transfer Functions: •OH Formation. *J. Electrochem. Soc.* **2017**, *164*, E3321. [CrossRef]

83. Negahdar, L.; Zeng, F.; Palkovits, S.; Broicher, C.; Palkovits, R. Mechanistic Aspects of the Electrocatalytic Oxygen Evolution Reaction over Ni-Co Oxides. *ChemElectroChem* **2019**, *6*, 5588–5595. [CrossRef]

84. Amadelli, R.; Maldotti, A.; Molinari, A.; Danilov, F.I.; Velichenko, A.B. Influence of the electrode history and effects of the electrolyte composition and temperature on O_2 evolution at β-PbO_2 anodes in acid media. *J. Electroanal. Chem.* **2002**, *534*, 1–12. [CrossRef]

85. Wang, C.; John Appleby, A.; Little, F.E. Electrochemical study on nano-Sn, $Li_{4.4}Sn$ and $AlSi_{0.1}$ powders used as secondary lithium battery anodes. *J. Power Sources* **2001**, *93*, 174–185. [CrossRef]

86. Guo, F.; Ye, K.; Du, M.; Huang, X.; Cheng, K.; Wang, G.; Cao, D. Electrochemical impedance analysis of urea electro-oxidation mechanism on nickel catalyst in alkaline medium. *Electrochim. Acta* **2016**, *210*, 474–482. [CrossRef]

87. Wan, T.H.; Saccoccio, M.; Chen, C.; Ciucci, F. Influence of the Discretization Methods on the Distribution of Relaxation Times Deconvolution: Implementing Radial Basis Functions with DRT tools. *Electrochim. Acta* **2015**, *184*, 483–499. [CrossRef]

88. Ciucci, F.; Chen, C. Analysis of Electrochemical Impedance Spectroscopy Data Using the Distribution of Relaxation Times: A Bayesian and Hierarchical Bayesian Approach. *Electrochim. Acta* **2015**, *167*, 439–454. [CrossRef]

89. Effat, M.B.; Ciucci, F. Bayesian and Hierarchical Bayesian Based Regularization for Deconvolving the Distribution of Relaxation Times from Electrochemical Impedance Spectroscopy Data. *Electrochim. Acta* **2017**, *247*, 1117–1129. [CrossRef]

90. Wang, Q.; Hu, Z.; Xu, L.; Li, J.; Gan, Q.; Du, X.; Ouyang, M. A comparative study of equivalent circuit model and distribution of relaxation times for fuel cell impedance diagnosis. *Int. J. Energy Res.* **2021**, *45*, 15948–15961. [CrossRef]

91. Zhang, X.; Song, W.-L.; Wang, M.; Tu, J.; Jiao, H.; Jiao, S. Photo-electrochemical enhanced mechanism enables a fast-charging and high-energy aqueous Al/MnO_2 battery. *Energy Storage Mater.* **2022**, *45*, 586–594. [CrossRef]